IOSR Journal of Applied Physics (IOSR-JAP)
e-ISSN: 2278-4861.Volume 10, Issue 4 Ver. I (Jul. – Aug. 2018), 57-76
www.iosrjournals.org

Oscillators with Nonpolar Magnetic Repulsion System and its Use in Rotary Nonresonant and Resonant Kinetic Energy Harvesters

Lukas Kurmann[1], Yu Jia[2]
[1]*IMTEK, University of Freiburg, Germany*
[2]*University of Chester, United Kingdom*

Abstract: *Creating an asymmetric torque signal over one full rotor revolution can be achieved when using a two degree of freedom (2DoF) system having a rotary and a translatory DoF andusing accordingly nonpolar magnetic repulsion techniques. This topic generally is popular in gray literature and is scarcely covered in peer reviewed scientific publications, as it often leads to the topic of permanent magnet motors, driven only by nonlinear magnetic spring configurations on the rotor and stator system, where the conservation of energy is violated. In this paper this problem is briefly discussed, while the focus is set to model the differential equation system and mathematically explore some of its major behaviors and properties. A working example of an existent magnetic motor is presented (the famous patented Yildiz permanent magnetic motor [1]). At first, a nonresonant rotary single DoF system will be modeled and discussed in detail. With two different methods an asymmetric torque signal is verified over one full rotor revolution using nonpolar magnetic repulsion techniques. Following on, a 2DoF system is modeled, in which both DoF resonate mutually together and exhibit at least one stable resonant frequency. The presented work hints to the working principle of the Yildiz motor macroscopically – an asymmetric and incommensurable rotor torque generation described by two mutually displacement coupled Mathieu equations – where the seemingly perpetual oscillation of such a system is sustained. However, the dynamics of such oscillators must be regarded as a modeling artefact as no microscopical explanation can be given of the energy conversion process nor a working prototype can yet be presented.*

Keywords -*Parametric Resonance, Nonpolar Magnetic Repulsion, Kinetic Energy Harvesting (KEH)*

Date of Submission: 02-07-2018 Date of acceptance: 18-07-2018

I.Introduction

Energy Harvesting is a technology for capturing non-electrical energy from ambient energy sources, converting it into electrical energy and storing it to power wireless electronic devices[1], [2], [3]. The process of capturing mechanical energy such as shocks and vibrations is a particular field of energy harvesting requiring specific types of energy harvesting devices, so called kinetic energy harvesters (KEH) [4], [5], [6]. This work originated from conventional electromagnetic (EM) vibration KEH's, where a suspended proof mass on a nonlinear spring is basepoint excited using nonpolar magnetic repulsion techniques [7]. Such SDoF transducers (first generation types) can harvest mechanical vibration energy effectively only in a narrow frequency window. Exploring transducer systems with more than one DoF might exhibit parametric and autoparametric resonance [7], [8], [9], [10] and have been investigated more recently (second generation types). During examinations of such (mainly 2DoF) resonator systems, also a rotary KEH system that uses nonpolar magnetic repulsion techniques has been studied, which exhibits strange seemingly perpetual motion behavior. The existence of at least one such physical model, presented also at the TU Eindhoven [11], the Yildiz motor, can scientifically always be questioned, as no scientist, nor at the TU Eindhoven (among others Dr. Backx and Dr. Duarte), nor Dr. Turtur had the chance to examine and measuring the device thoroughly; however, a European patent has been granted [12] and basic load measurements at the TU Eindoven were made (see also section X). This manuscript hints at least a macroscopic explanation, why such strange phenomena might be possible. We use still the naming convention KEH device, as effectively rotor mass and rotor inertia are used to start a seemingly perpetual oscillation in such a device. Microscopically, there might be yet unknown sources why such apparent perpetual motion is possible [11]. Chapter II shows the modeling of an unbalanced torque signal using nonpolar repulsion techniques, and chapter III applies such permanent magnet (PM) spring systems in an SDoF oscillator system using a cam. In chapter 4 we use instead of a cam, an additional DoF and investigate a 2DoF oscillator system.

II. Creating A Numerical Model For Simulating An Unbalanced Torque Signal

Using the finite element(FE) tool COMSOL and modeling nonpolar magnetic repulsion systems magneto-statically (magnet fields no currents), force and torque signals for such systems can easily be extracted and validated. Let us look first at one pair of disk PMs in repulsive magnetic configuration, shown in Fig.1a. Such a pair is formed with an outer disk PM(1) on a stator in the reference frame and an inner rotor disk PM (2) fixed on a shaft that can rotate in ϕ direction and move along the z axis. Disk PM magnet dimensions for stator and rotor are designated with $\emptyset d_{S,R}$ (disk diameter) and $h_{S,R}$ (disk height). Fig.1b shows a similar setup, but four PM pairs on the stator-rotor system are used. The stator (1) and rotor (2) are placed symmetrical at the origin O, z axis outwards of the page and cross section $A-A$ displayed to show translatory rotor movement. Similar setups with different number of stator-rotor PM disk magnet pairs are shown later in Fig.9, Fig.12 and Fig.23.

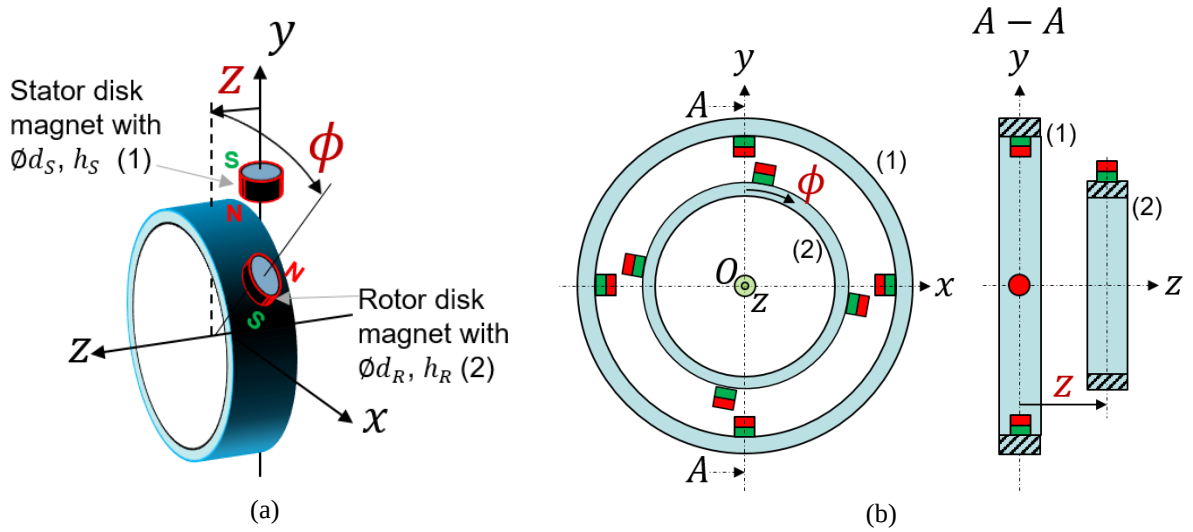

(a) (b)

Fig.1. 2DoF rotary-translatory shaft movement with one stator-rotor disk PM magnet pair (a) and four symmetrically placed stator-rotor disk PM pairs (b) with PM disk geometry $\emptyset d_{R,S} h_{R,S}$.

To compute the torque and force signal of the magnet pair(s)acting on the rotor from Fig.1 is of interest. The torque and force of the moving rotor PM is calculated by using the integral of the surface stress tensor. The boundary normal vector pointing out from the PM is $\boldsymbol{n}$, σ the stress tensor, the resulting torque vector $\boldsymbol{\tau}$, its amplitude τ and the resulting force vector $\boldsymbol{F}$(amplitude F) created by integrating over all boundary elements dS, (1), (2), see also [13].

$$\boldsymbol{F} = \int_{\partial\Omega} \boldsymbol{n}\, \sigma\, dS \tag{1}$$

$$\boldsymbol{\tau} = \boldsymbol{r} \times \boldsymbol{F} \tag{2}$$

Fig.2 shows the resulting FE calculated torque and force signals for one and four stator-rotor PM pairs (from Fig.1). This FE calculated torque and force signal can be, for instance, approximated with a 4^{th} order Fourier series. Using a 4^{th} order series, to make sure that the error in the force and torque interval is small. A normalized Fourier approximated signal for radial torque signal $f_{\tau rad}(\phi)$(3) and for axial force signal $f_{Fax}(z)$(4) can be generated having used only sin terms, as we know that both functions must be odd.

$$f_{\tau rad}(\phi) \cong \sum_{n_\tau=1}^{4} b_{n_\tau} \sin\left(n_\tau \omega_{\phi_\tau}\, \phi\right) \tag{3}$$

$$f_{Fax}(z) \cong \sum_{n_f=1}^{4} b_{n_f} \sin\left(n_f \omega_{\phi_f}\, z\right) \tag{4}$$

The rotary stiffness term C_r $(Nmrad^{-1})$ and the axial stiffness term $k_r(Nm^{-1})$. might be later measured using only one single stator-rotor PM pair. The resulting rotor torque- and force-signal can therefore be written as (5), (6). These equations correspond to the blue lines of Fig.2. In case where four, point symmetrical PM pairs are used (Fig.1b), the resulting torque and force signal is simply the fourfold of the factor C_r respectively k_r (shown with the red lines in Fig.2).

$$\tau_{rad}(\phi) = C_r f_{\tau rad}(\phi) \tag{5}$$

$$F_{ax}(z) = k_r f_{Fax}(z) \tag{6}$$

On the rotor circumference, only a limited number of disk PM pairs can be placed in the same $\phi - z$ plane – due to the rotor diameter and the PM geometry. However, as such PM pairs can be placed on consecutive $\phi - z$ planes, theoretically an arbitrarily high torque and force signal can be created.

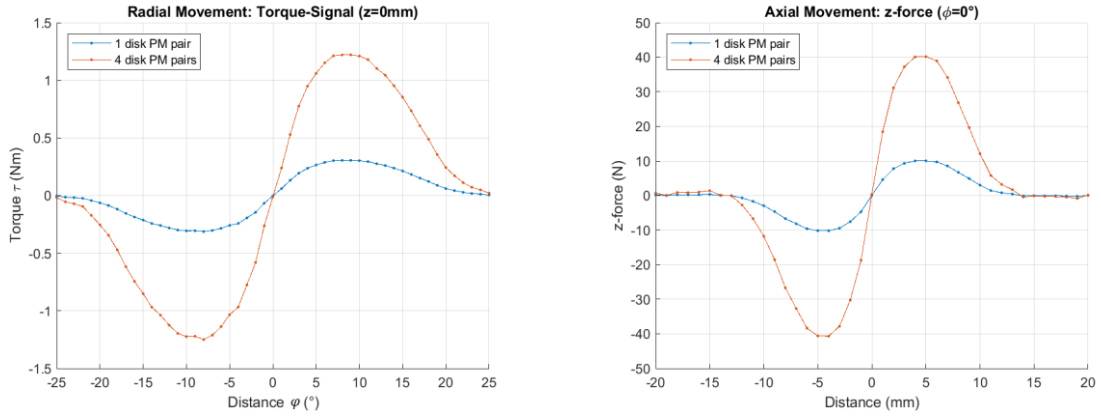

(a) (b)

Fig.2. FE simulated rotary shaft torquewith one and four rotor-stator disk magnet pairs (a)and the axial force signal (b). The same geometry and magnetization for all PM pairs used (air gap of PM magnet pair is kept1mm for all simulations; N52 disk magnets used$d_R = d_S = 10mm$ and $h_R = h_S = 5mm$); radiusr_0 from origin to the center of mass of the moving rotor PMs$r_0 = 27mm$.

Diagrams of Fig.3a show again the same FE simulated torque signal τ_ϕ (blue signal) and its 4th order Fourier series approximation (red signal) using approximation (3). For these (blue and red) signals, the corresponding designated x axis 'Angle ϕ (°)' is valid. A brief description of the physical meaning of this signal: there needs to be mechanical torque energy pumped into the rotor, reaching the maximal negative torque of $\tau_{max\,-} \cong -0.305Nm$ at $\phi \cong -8°$ and reaching at $\phi = 0°$ the instable point where for $\phi > 0°$ rotor starts accelerating until reaching $\tau_{max\,+} \cong +0.305Nm$ (with maximal velocity close to $\phi = 26°$).

Also depicted in diagrams of Fig.3a is the torque envelope signal denoted with τ_z. It is also created by using first an FE computed torque signal (orange curve; keeping the torque angle at its maximum $|\phi| \cong 8°$ and sweeping subsequently with this fixed torque angle) in the axial z direction. This created torque envelope function $\tau_z$must be an even function; like in the $f_{\tau rad}(\phi)$ case, also an approximated 4th order Fourier series is used $f_{\tau ax}(z)$(7), with coefficients a_{n_τ} and ω_{z_τ} to finally create the correspondingtorque signals (red and violet curves).

$$f_{\tau ax}(z) \cong a_{0_\tau} + \sum_{n_\tau=1}^{4} a_{n_\tau} \cos\left(n_\tau \omega_{z_\tau} z\right) \tag{7}$$

A 3D torque amplitude diagram can be realized, when combining both degrees of freedom ϕ and z together, shown in Fig.3b. This normalized function is the product of τ_ϕ and τ_z, e.g. the product of (3) and (7), given in (8). This function $f_\tau(\phi, z)$ characterizes the normalized 2D torque function.

$$f_\tau(\phi, z) \cong f_{\tau rad}(\phi) f_{\tau ax}(z) = \left(\sum_{n_\tau=1}^{4} b_{n_\tau} \sin\left(n_\tau \omega_{\phi_\tau} \phi\right)\right)\left(a_{0_\tau} + \sum_{n_\tau=1}^{4} a_{n_\tau} \cos\left(n_\tau \omega_{z_\tau} z\right)\right) \tag{8}$$

The correspondent normalized 2D force function is created analog the above presented torque function. The equation (9) gives the normalized force signal in radial direction, again for physical reasons, it must be an even function, here also given as a 4th order Fourier series approximation expression.

$$f_{Frad}(\phi) \cong a_{0_f} + \sum_{n_f=1}^{4} a_{n_f} \cos\left(n_f \omega_{z_f} \phi\right) \tag{9}$$

Like in Fig.3b, in Fig.4bthe 3D forceamplitude diagram is realized, combining both degrees of freedom ϕ and z together. This normalized function is the product of F_z and F_ϕ e.g. the product of (4) and (9), given in (10).

$$f_F(\phi, z) \cong f_{Fax}(z) f_{Frad}(\phi) = \left(\sum_{n_f=1}^{4} b_{n_f} \sin\left(n_f \omega_{\phi_f} z\right)\right)\left(a_{0_f} + \sum_{n_f=1}^{4} a_{n_f} \cos\left(n_f \omega_{z_f} \phi\right)\right) \tag{10}$$

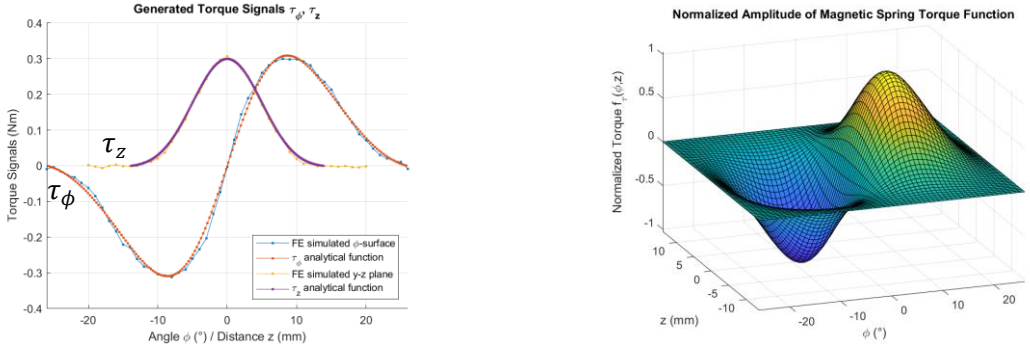

(a) (b)

Fig.3. Diagram (a) shows the FE simulated torque signals inϕ- and z-direction and its 4th order Fourier series approximated equivalent signal. Diagram (b) shows the resulting normalized torque amplitude plot given in (8).

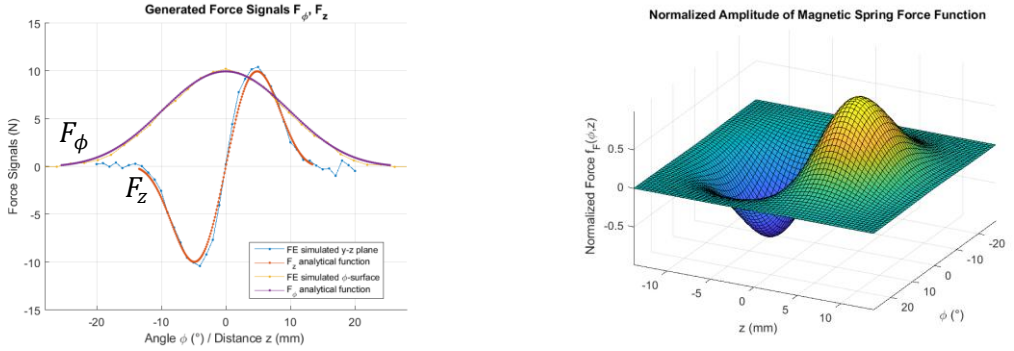

(a) (b)

Fig.4. Diagram (a) shows the FE simulated force signals inϕ- and z-direction and its 4th order Fourier series approximated equivalent signals. Diagram (b) shows the resulting normalized force amplitude plot given in (10).

Fig.4 shows FE simulated force signals and its corresponding normalized 3D spring force function. This function looks like the torque function – but we deal in this plane with a force and not a torque signal and the PM alignment and its resulting force function is slightly different, as the PM are not rotating radially, but sliding axially (as shown in Fig.1c and Fig.1d). The envelop-function (F_ϕ) and the x force component (F_z) create like the torque function, a 3D force amplitude graph, in (b) shown normalized.

The Fig.3b and Fig.4b can also be represented in a more compact way using a vector field plot. For each doublet ϕ, z, a corresponding vector representation for $\tau$and F can be created.

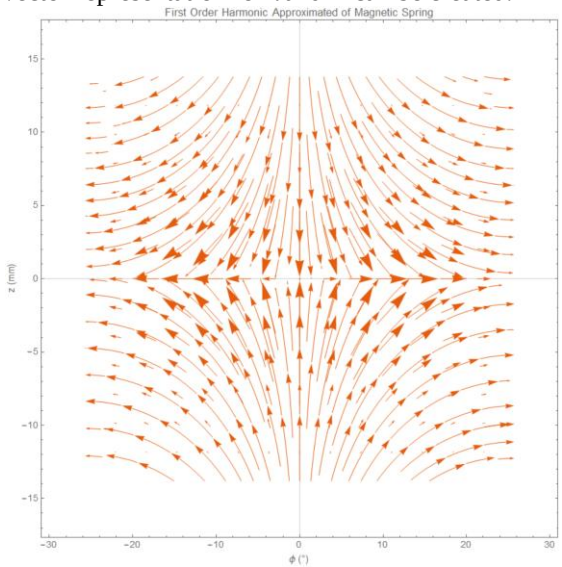

Fig.5. 2D vector field representation of 2D torque and force function, combining of Fig.3b, Fig.4b.

Fig.6a depicts a distribution of disk PMs used in a FE simulation environment to simulate statically the resulting torque on the six (inner) rotor magnets that sit on an imaginary rigid shaft (not shown in this sketch). The sketch of Fig.6b shows in the developed view ($\phi - z$plane) in green and blue the same stator-rotor disk

PMconfiguration. The gray large circles outside the green and blue dots sketch the approximated influence of the magnet field of each permanent magnet. The light blue dot shows the beginning of the next 2π periodic PM surface distribution (at zero degree the stator and rotor PM are superimposed and only the rotor magnet is visible – behind there is the stator PM present).

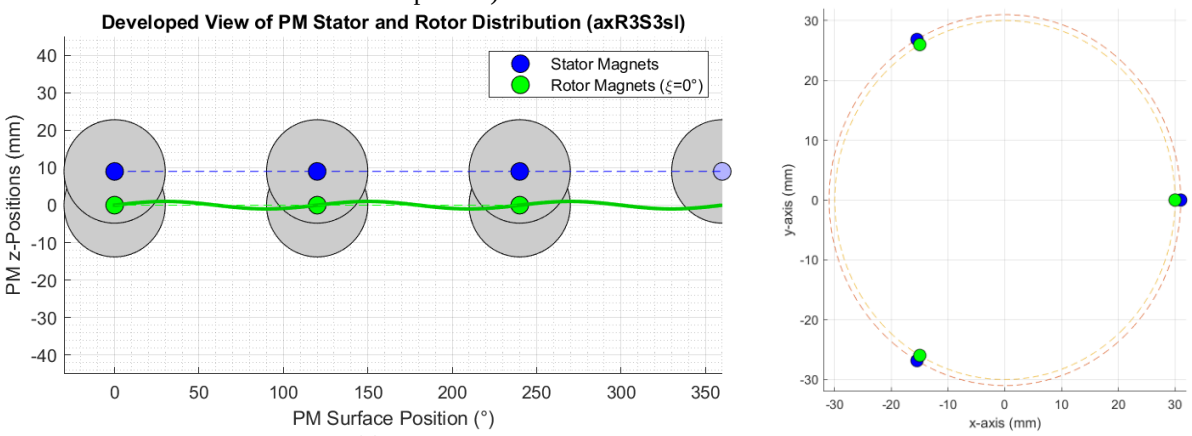

(a) (b)

Fig.6. Diagrams show an axial PM configuration (ax) with 3 rotor PMs (R3) and 3 stator PMs on a single line (S3sl), PM distribution naming nomenclature given axR3S3sl. Diagram (a) shows developed view of PM distribution on the radial surface ϕ and z. Diagram (b) the same system in x-y axis direction.

If we keep for this PM configuration the rotor z-axis constant while moving along ϕ, we will obtain evidently always a resulting sum torque of zero over one full revolution. However, when the rotor in z-direction is swayed as a function of angle ϕ (this is also called a cam function), a torque signal unequal zero (over one revolution) can be obtained. Equation (11)gives a simple harmonic example functionfor such a z movement dependency; z_R is the resulting rotor movement when ϕ is moved from 0 to 2π, with a given amplitude $A$and an initial offset angle ξ_o.

$$z_R(\phi) = A\sin(\omega_n\ \phi + \xi_o) \tag{11}$$

Applying such a cam function, and setting parameters$A = 1mm$ and $\xi_o = 0°$ and $\omega_n = 3$, a positive torque signal over one 2π period cycle can easily be reached. The shown cam function of (11) has been first tested with an analytical model by evaluating (8) for each rotor magnet the z and ϕ distance to all stator PM's over one full revolution with which the resulting torque for this rotor PM element can be obtained. This evaluation is done for all PM magnets on the rotor to find the overall net torque of this stator-rotor PM configuration. The verification is done by comparing the analytically obtained result with the static magnet field FE calculation over one full revolution.This FE calculation is computationally intensive and ca. 6000-times slower to compute (on a standard PC it takes ca. $1h$).

This verification is shown inFig.8. The red line is the analytically obtained calculation using the magnetic torque spring function (8)and the blue line shows the obtained FE simulated counterpart. Both curves have a similar form and follow each other well. There are two parameters which are important: one is the overall created net torque $\sum\tau$magnitudeand its positivity, where for $> 50\%$, a positive torque is achieved and $< 50\%$ a negative net torque is present. In this presented calculation, the static calculated FE simulation, shows even a slightly larger positive torque magnitude and a larger positivity than its analytically obtained counterpart calculation. A torque different from 50% can easily be reached with many different geometry configuration and cam functions. For creating an asymmetric incommensurable torque signal, it is important to align the harmonic axial rotor movement with the PM configuration.

Having an analytical spring function, optimization can be done easily and the issue can be reduced to multivariable optimization problem. A first, none exhaustive optimization was done, by regarding the PM stator magnet distance as an optimization parameter. This optimization is shown in a sweep-plot in Fig.7b, where for one full revolution the PM distance to the origin is changing between 0…20mm. The result in Fig.7a is shown for an offset of stator PMs of 9mm (to the origin, compare also Fig.6a). The three resulting torque curves $\tau_{1\ldots3}$ cumulate the net torque at the same spots over one full revolution. The resulting sweep shows that for no asymmetric z distance (e.g. PM z-Position 0mm) a symmetric torque results. Also, for large distances >15mm, no torque is produced, as PM repulsion spring influence is cut off. For offset distances between 1 and 15mm, the net torque is given in red and the asymmetric percentage in blue (Fig.7b).

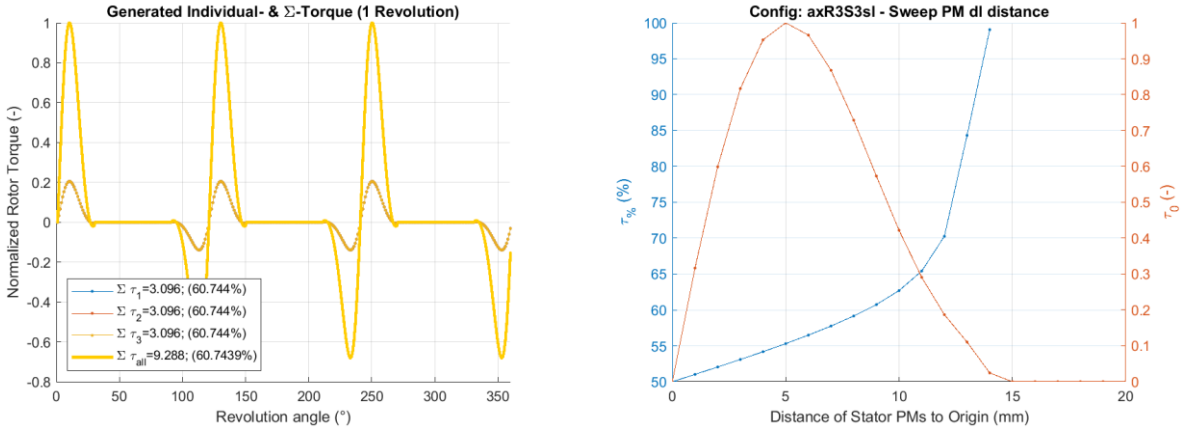

(a) (b)

Fig.7. Diagram a depicts generated normalized torque signals with analytical torque simulations (orange) and diagram b shows a stator PM sweep from 0…20mmand the resulting torque signals in % (left axis) and normalized (right axis). A torque of all summed up 3 rotor disk PMs is clearly positive (> 60%).All used PMs have same geometry and magnetization strength of stator and rotor PMs (PM parameters given in caption of Fig.2).

Fig.8a shows the FE setup and Fig.8b the verification of the analytical generated torque signal given in Fig.7a. For both calculation methods, the same clearly positive torque signal is generated.

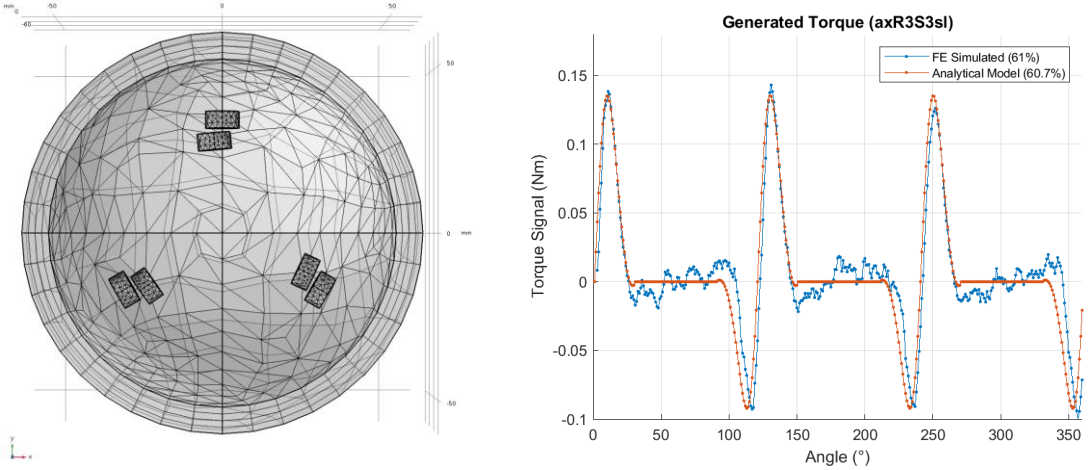

(a) (b)

Fig.8. Diagram (a) a shows FE mesh model built according setup of Fig.6. Diagram (b) shows generated torque signals with FE simulation (blue) and analytically approximated (red). In both cases, net torque of all summed up rotor disk PMs is positive (61%) over one full revolution; peak torque is reached at 10°, 130° and 250° with torque maxima of ca. 0.135Nm using analytical model with calculations using equation (8). FE model shows same behavior, resulting in same averaged peak torque of 0.135Nm.

It is most interesting, that with a given geometrical stator-rotor PM distribution, an arbitrarily complex torque curve over one full revolution can be generated. Note also, that making this analytical simplified numerical model, it will rest an approximated signal and a magnetostatical FE simulation verification is indispensable. In this manuscript, we restrict the investigation of asymmetric torque signals using an additional axial movement. Instead of such an axial movement, also a radial movement can be envisaged.

III. Nonresonant Oscillator Using An Axial Cam

3.1 Lumped parameter model

Fig.9 shows the lumped parameter model. A rotating disk, the rotor with inertia J and mass m, is spinning radially with $\phi(t)$ and moving axially with $z(t)$. On diagram (b) an EM transducer circuit is shown with 3 coils wound around the stator PM setup. The circuit in the electrical domain consists of the transducer u_{emf}, the copper resistance of the coils$R_{coil\,1\ldots3}$ with its sum inductance $L_{coil\,1\ldots3}$ and the resistive load R_{load} andthe stator-rotor PM setup has the same configuration as shown in Fig.8b.

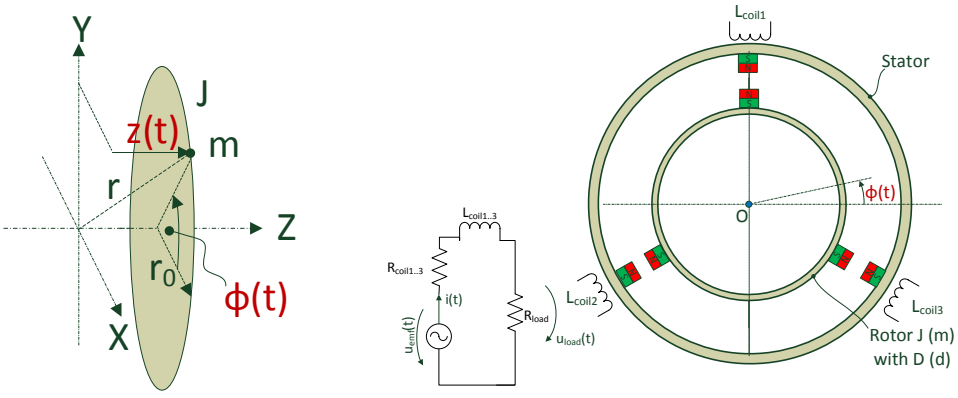

(a) (b)

Fig.9. Model of a 2DoF disk rotating radially with angle $\phi(t)$ and moves axially with $z(t)$ (a). Diagram (b) shows the lumped parameter model including transducer systems on the stator. The stator-rotor distribution might be the one shown in Fig.6 or the one in Fig.8b.

Equation (12) gives the vector $r(t)$ in Cartesian coordinates from the origin to the mass point m on the disk radius r_0 and the axial z distance$z(t)$.

$$r(t) = \begin{pmatrix} r_0 \sin\phi(t) \\ r_0 \cos\phi(t) \\ z(t) \end{pmatrix} \tag{12}$$

Deriving the corresponding governing differential equation (DE) system, we are applying the Lagrangian formalism (13), (14) and obtain the kinetic energy T of the system (15).

$$L = \frac{d}{dt}\left(\frac{\partial L}{\partial \dot{q}_i}\right) - \frac{\partial L}{\partial \mathrm{q}_i} = 0 \tag{13}$$

$$L = T - U \tag{14}$$

$$T = \frac{1}{2} m \left(r'(t)\right)^2 = \frac{1}{2} m\, z'(t)^2 + \frac{1}{2} J\, \phi'(t)^2 \tag{15}$$

The friction term D for the torque and d for the force DEare inserted separately in this non-conservative DE system. Both friction terms are functions of $\phi'(t)$ and $z'(t)$, e.g. $D\left(\phi'(t)\right)$and $d\left(z'(t)\right)$ following [14]. For simplicity we denote them as D and d, knowing that they are functions of the velocity signals. The stiffness terms C and k could be obtained if a potential U can be found. An attempt was made to obtain such a spring potential, but it could not be applied successfully, see also appendix chapter VII.The stiffness terms are functions dependent of ϕ and z. Inserting these normalized stiffness's for torque and force signals $f_\tau(\phi, z)$ and $f_F(\phi, z)$ (see also Fig.3b and Fig.4b) with their corresponding amplitude constants C and k, add the additional mechanical (viscous) damping from the electrical circuit – the transducer constant $\varepsilon_{\phi,z}\, i(t)$ times the current i, the system can be written as follows:

$$J\, \phi''(t) + D\phi'(t) + C\, f_\tau(\phi(t), A\sin(\phi(t) + \xi_o)) + \varepsilon_\phi\, i(t) = 0 \tag{16}$$

$$m\, z''(t) + dz'(t) + k\, f_F\left(\arcsin\left(\frac{z(t)}{A}\right) - \xi_o, z(t)\right) + \varepsilon_z\, i(t) = 0 \tag{17}$$

$$L_{coil\,1\ldots3} i'(t) + (R_{coil\,1\ldots3} + R_{load}) i(t) = \varepsilon\, \phi(t) \tag{18}$$

As $z(t)$ is a dependent cam parameter of$\phi(t)$, (11) is inserted into $f_\tau$to obtain (16). In (17), parameter $\phi(t)$ of f_F has been replaced with $z(t)$ using the inverse function of (11). Another way to write (17) is, replacing $z(t)$ with $\phi(t)$ (and their derivatives) using (11):

$$\begin{aligned} m\, A\, (-\sin(\phi(t) + \xi_o)\phi'(t)^2 + \cos(\phi(t) + \xi_o)\phi''(t)) + d\, A\cos(\phi(t) + \xi_o)\phi'(t) \\ + k\, f_F(\phi(t), A\sin(\phi(t) + \xi_o)) = 0 \end{aligned} \tag{19}$$

The seemingly complex torque displacement term of (16) is a 1D curve which might have a 2π periodicity, depending on the used stator-rotor PM configuration (Fig.7 shows for instance such a sample curve). In the next chapter, we use (16) and (18) and assume that the axial cam friction is small. This cannot safely be assumed, as additional mechanical friction from the cam will be present (additional friction like air drag in both cases not considered).

3.2 Time domain response

Figure 12 shows the top-level block diagram of MATLAB Simulink implementation of DE system (16) and (18). The shown damping characteristic for this model is depicted in red ´Damping Models´ (one of the 3 different friction models can be selected). The damping feedback of the electrical domain into the mechanical domain is shown with a blue amplifier block named ´coilCoupling2´ (corresponding transducer constant times electrical current $\varepsilon_\phi i$). In the following simulations, the feedback loop has been set zero, e.g. $\varepsilon_\phi i = 0$. A simple mechanical SDoF system is given with only a radial moving mass and inertia J, a nonlinear mechanical friction and an elaborate stiffness term (see for example Fig.7 implemented via a lookup table).

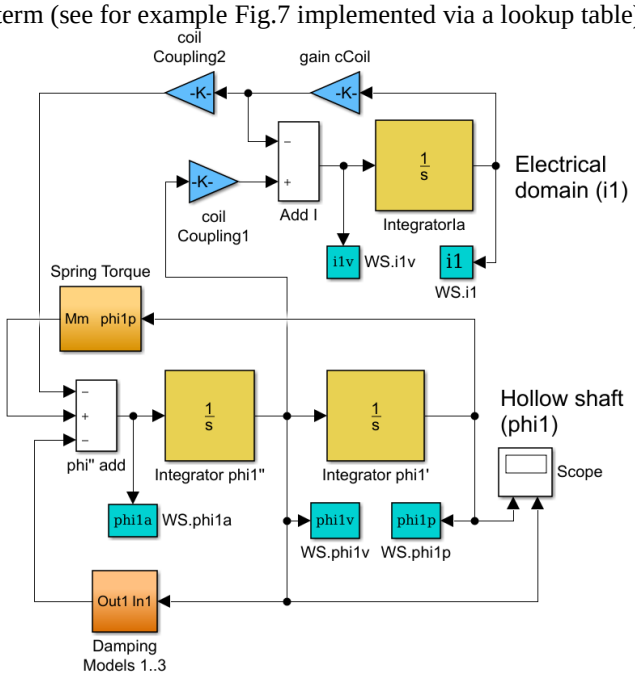

Fig.10. Top level implementation of DE set (15) and (17) in MATLAB Simulink.

In Fig.11, the motion signals (ϕ_1, ϕ_1') of a rotor with an axial harmonic cam(11) and parameters A =1mm, $\omega_n = 3$ and $\xi_o = 0$is shown, including also the normalized stiffness signal ($T_{mag\ norm}$). In such a case an apparent perpetual rotor motion is generated. The final angular velocity steady state signals are highly dependent of the chosen stator-rotor PM distribution and the friction of a given cam.Generating a harmoni cam with $\omega_n = 3$that absorbs not too much of friction and has a profile as shown in Fig.7a (see also Fig.8b or Fig.11 pink line) is only difficult to realize. A more realisitc cam should have only one single period per revolution, e.g. $\omega_n = 1$ or at least an amplitude which is smaller.

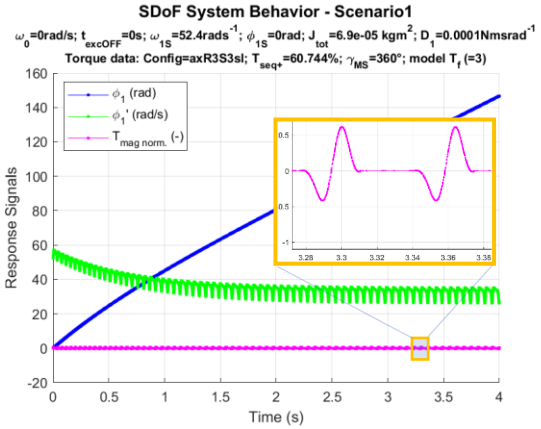

Fig.11. Initial condition of rotor movement is $\omega_{1S} = 400 min^{-1}$ (see also parameter settings in subheadings). The shown system behavior of an axial cam movement and PM distribution from Fig.7a with rotor displacement ϕ (blue) and its angular velocity (green) oscillating with steady state angular velocity oscillation $26.3\,rad/s < \omega < 35.2\,rad/s$. A nonlinear friction model $T_f (= 3)$ of [14] for this rotary SDoF system has been applied.

Note also, that such a distribution can be arbitrarily repeated over the stator and rotor system and therefore overcome principally any rotary friction (D_1). Furthermore, such apparent perpetual rotor motion can only be achieved when a kinetic start energy $T_{1S}(20)$ is greater or equal than the equivalent applied maximal angular steady state velocity oscillation $\omega_{max} = \phi'_{max}$.

$$T_{1S} = \frac{1}{2} J \, \phi'^{2}_{max} \tag{20}$$

$$\omega_{1S} \geq \omega_{max} = \phi'_{max} \tag{21}$$

IV. Resonant Oscillator Using Magnetic Spring

4.1 Lumped parameter model

Let us consider the case with no cam function and both DoF can oscillate freely. The lumped parameter model for such a KEH system is depicted in Fig.12. For this system, six symmetric stator PMs are drawn (they could represent also a stator PM distribution shown in Fig.13 with two rows of 6 PMs) and on the rotor two symmetrical placed PMs are present. In addition, also axially in z direction two sets of PMs are present. The inner PMs (A) are fixed on the rotor and this system ((A) and rotor) can slide in the hollow shaft axially (along the z axis) and the outer PMs (B) are fixed on the hollow shaft which rotates in the x-y plane. z_{asym} denotes the distance from origin O to the symmetry axis of the off-centered rotor system.

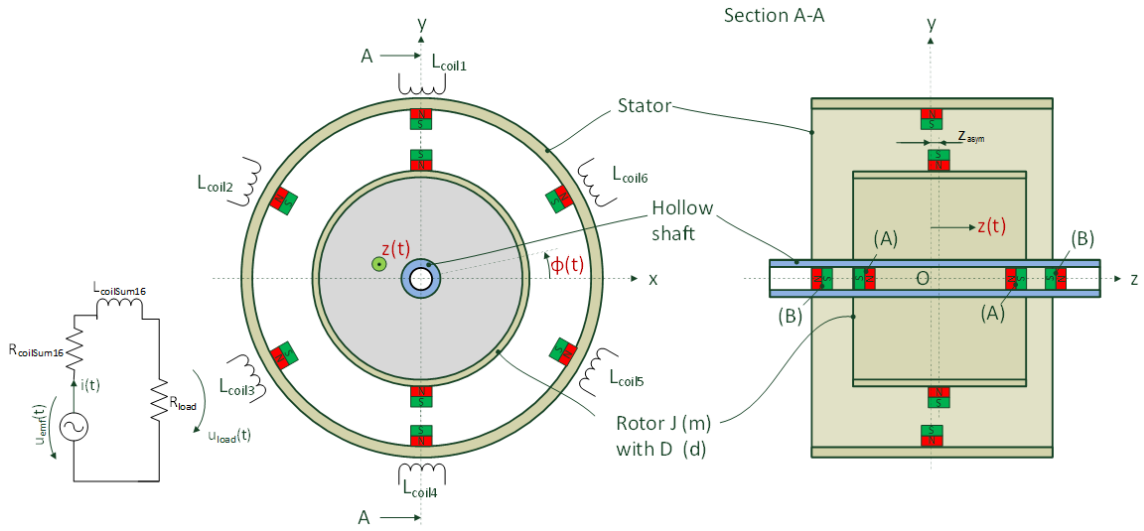

Fig.12. Lumped parameter model of 2DoF KEH system with a rotating $\phi(t)$ axially $z(t)$ moving rotor on a hollow shaft is drawn without no bearings. A transducer might be present, electrical domain shown in the lower left-hand side corner.

The resulting model, which has been already developed in chapter III, can be written as shown in DE system (23), (24) and (25).Independent variables are $\phi(t)$ and $z(t)$ with inertia J and mass m, as already derived in (16) and (18). Also, the mechanical damping terms D and d are present and realized with a nonlinear, e.g. stick-slip friction model[14]. The stiffness functions are more elaborately modeled compared to (16) and (18). No fixed periodic torque and force function can be assumed, but for each PM spring the sum of all torque and force signals over one complete 2π cycle is modeled. The normalizedf_τ, f_F functions represent the torque and force components of the stator spring system (over one 2π period). The rotor magnets are placed at ϕ_n and z_n. The stiffness term C_r amplifies the torque sum of all magnets present in the system n_{PM}. The same setup is done for the force functions in the force DE (24), where k_r represents the axial spring stiffness amplitude and k_1 and k_3 the corresponding linear and nonlinear stiffness parameters of the axial spring system (in Fig.12, section A-A depicted with (A) and (B)). Transducers on the stator might add additional viscous damping to the corresponding DE, here present with the according transducer parameters ε_ϕ and ε_z for the radial and axial component.

The potential $U$of the axial spring is known (22) and applying the Lagrangian formalism (13), (14), we obtain the terms $k_1 z + k_3 z^3$ of (24). This 3rd order polynomial approach is beneficial when dealing with

nonlinear spring system, see for example [15]. Note that U represents solely the axial spring potential – a spring potential for the radial spring system could not be obtained successfully (appendix chapter VII). In case the rotor is driven forced, the angular velocity ω_0 is unequal zero.

$$U = \frac{1}{2}k_1(z - z_{asym})^2 + \frac{1}{4}k_3(z - z_{asym})^4 \tag{22}$$

$$J\phi'' + D\,(\phi' - \omega_0) + C_r \sum_{n=1}^{n_{PM}} f_\tau(\phi - \phi_n, z - z_n) + \varepsilon_\phi i = 0 \tag{23}$$

$$mz'' + dz' + k_r \sum_{n=1}^{n_{PM}} f_F(\phi - \phi_n, z - z_n) + k_1\,(z - z_{asym}) + k_3(z - z_{asym})^3 + \varepsilon_z i = 0 \tag{24}$$

$$L_{coilSum\ 16}\,i' + (R_{coilSum\ 16} + R_{load})i = \varepsilon_\phi \phi + \varepsilon_z z \tag{25}$$

One configuration of the stator spring system is depicted in Fig.13. The developed stator surface for torque (a) and force (b) functions is given here for the radially placed PM batteries. The shown plots are simply a Lego-like placed summation plot, composed of 12 disk PMs (see corresponding equations (8), (10)and Fig.3b, Fig.4b). The radial PMs correspond to the distribution on the stator in the x-y plane of Fig.12 and the axial magnets correspond to the PMs shown on the stator in the y-z plane (section A-A). The axial spring system is done simpler – only one z dependent direction for this spring setup is used (Fig.14a). Instead of only two nonpolar magnetic repulsion systems (see also Fig.12 section A-A, (A) and (B)) in the center of the z axis, also a more elaborated axial spring system might be present – in the same fashion as the radial spring system.

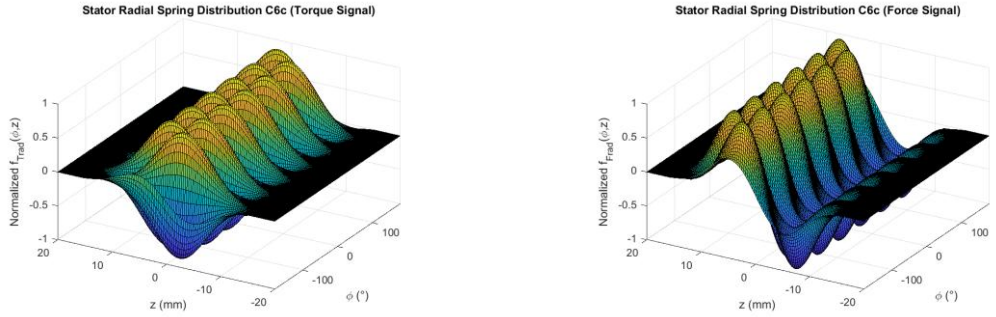

(a) (b)

Fig.13. Radial PM stator distribution with 2rows and 6 symmetrical distributed PM's over 360° (30° angle- and 10mm z distance-offset of each set). Diagram (a) shows torque signal and its corresponding force signal (b).

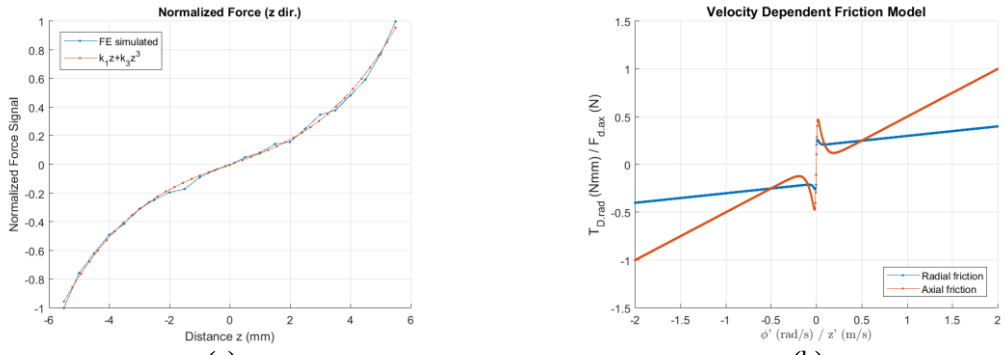

(a) (b)

Fig.14.Normalized force using a 3rd order polynomial approximation (a) and damping behavior for corresponding radial (blue) and axial (red) velocities (b).

The shown damping characteristic for this model is depicted in Fig.14. The implementation of the fundamentally simple nonlinear DE set (23), (24) and (25) is shown in Fig.15. The damping feedback of the electrical domain into the mechanical domain is shown with blue amplifier blocks named ´coilCouplingZ´ (corresponding$\varepsilon_z i$) and ´coilCouplingPhi´ (corresponding$\varepsilon_\phi i$). In the following simulations, both feedback loops have been set zero, e.g. $\varepsilon_\phi i = \varepsilon_z i = 0$. The 2D torque- and force-springs have been derived in (8) and (10). Its first order approximation can be written as (26) and (27).

$$f_\tau(\phi, z) \cong C_r b_{1_\tau} \sin(\omega_{\phi_\tau}\,\phi)\,(a_{0_\tau} + a_{n_\tau} \cos(\omega_{z_\tau}\,z)) \tag{26}$$

$$f_F(\phi, z) \cong k_r b_{1_f} \sin\left(\omega_{\phi_f}\,\phi\right)\left(a_{0_f} + a_{n_f}\cos\left(\omega_{z_f}\,z\right)\right) \tag{27}$$

Inserting (26) and (27) into DE system (23), (24)and setting both transducer constants zero $\varepsilon_\phi = \varepsilon_z = 0$, a simplified mechanical DE system can be obtained:

$$J\phi'' + D(\phi' - \omega_0) + C_r b_{1_\tau} \sin(\omega_{\phi_\tau}\,\phi)\left(a_{0_\tau} + a_{n_\tau}\cos(\omega_{z_\tau}\,z)\right) = 0 \tag{28}$$

$$mz'' + dz' + k_r b_{1_f} \sin\left(\omega_{\phi_f}\,\phi\right)\left(a_{0_f} + a_{n_f}\cos\left(\omega_{z_f}\,z\right)\right) + k_1\,(z - z_{asym}) + k_3(z - z_{asym})^3 = 0 \tag{29}$$

Inspecting, expanding (28) and (29), it follows that both DE have the form of damped Hill´s DE (where f_p denotes the periodic function generalized from the Mathieu DE where it is limited to harmonic functions):

$$q'' + dq' + q\left(a + f_p(t)\right) = 0 \tag{30}$$

Such DE have a most complex stability behavior – in this system of (28) and (29), they are additionally mutually coupled. This is most interesting and in the next section we will show that such oscillator systems might exhibit at least one mutually coupled stable resonance.

4.2 Time domain response

Simulation results with given radial PM stator distribution (resulting torque and force signal of Fig.13) are depicted inFig.16 – Fig.20. In those figure captions, first subheading shows initial conditions and axial impact range (impacting is used only in exceptions – implementation of such impacting described in appendix chapter IX, here set to $\pm 5.5mm$). Second subheading starts with rotor PM radial and axial distribution, f_{rad} and f_{ax}. Subscripts of those functions give the geometrical placing of the rotor magnets. For example, in Fig.16a all six radial magnets are placed in the center at $0mm$, whereas for the axial spring a 1D PM spring is placed. In Fig.16b, instead of an axial 1D PM spring, a 2D PM spring system is placed with three axial magnets on each side asymmetrically at $+25mm$ and three at $-27mm$ (see also appendix chapter VIII). Superscript of f_{rad} and f_{ax} give the radial and axial location in 10° intervals. In the legends of Fig.16 – Fig.20, ϕ_1, ϕ_1' and z_1, z_1' denotes the displacement and velocity signal ϕ, ϕ' (1st DoF) and z, z' (2nd DoF).

In simulation of Fig.16b, we have radially six symmetrical PMs placed and axially at each side three PMs (at 0°, 120° and 240°). z_a indicates that axial distribution is done asymmetrical (see also equation (24)) and followed by the stiffness factors$C_{rad,ax}$. The last subheading starts with ω_0, a potential excitation velocity and its time t_{excoff} – both set zero. The radial and axial damping main parameter is indicated with D_1 and d_1 (the additional damping parameters not shown (to create the damping behavior of Fig.14). Inertia and mass are also set realistically using 3D printing technologies.

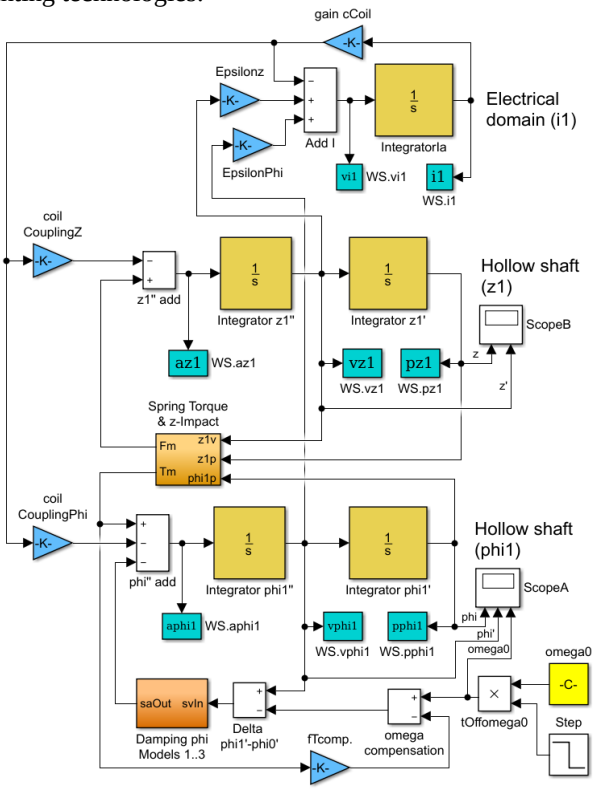

Fig.15.Top level implementation of DE set (23), (24) and (25) in MATLAB Simulink, where phi1, z1 and i1 represent ϕ, z and i.

The initial angular velocity is dropping steadily until a resonance on the z axis is hit at ca. 0.5s. The z displacement amplitude starts growing and a steady state oscillation is found and seemingly locked in to the ϕ radial movement. This simulation has been also simulated for much longer, up to$t_{sim} = 500s$. Several solvers (ode23 Bogacki-Shampine, ode23s Mod. Rosenbrock, ode45 Dormand-Prince) with set relative tolerance down to 10^{-12} were applied.

Figure 18 compares the oscillation characteristics of two different axial spring setups, one given in the lumped parameter model from Fig.12, the other from lumped parameter model from Fig.22. The steady state angular velocity oscillation is similar; in both cases the axial asymmetry offset is $2mm$, but a main difference comes from the different used disk PM geometries and therefore its different stiffness characteristics.

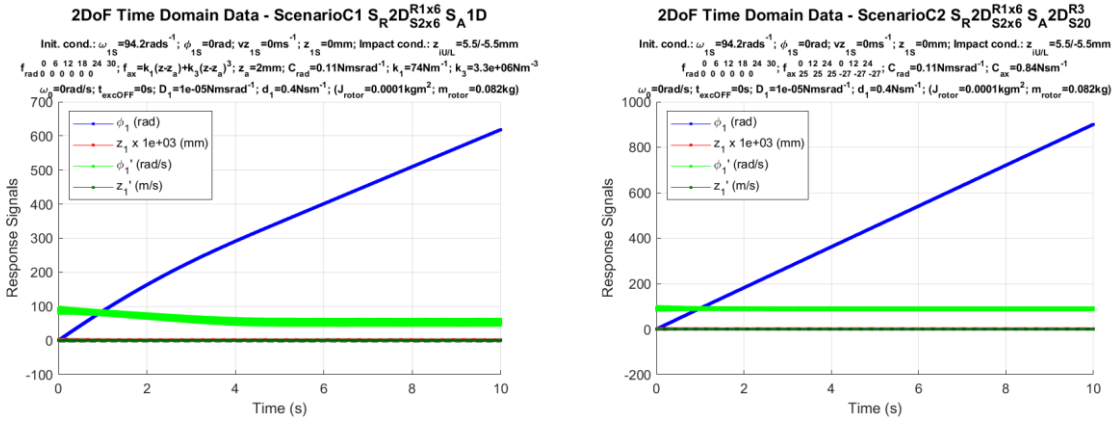

(a) (b)

Fig.16. Comparison of axial PM spring arrangements and its resulting oscillation characteristics (shown also as f_{ax} function in 2nd line of the corresponding subheading). In (a) with a 2D PM spring radial setup and a 1D PM spring axial setup (asymmetric placement $z_{asym} = 2mm$) from Figure 14 is used whereas in (b) a different axial spring setup from Fig.22 is in place (a 2D PM spring radial setup and a 2D PM spring axial setup).

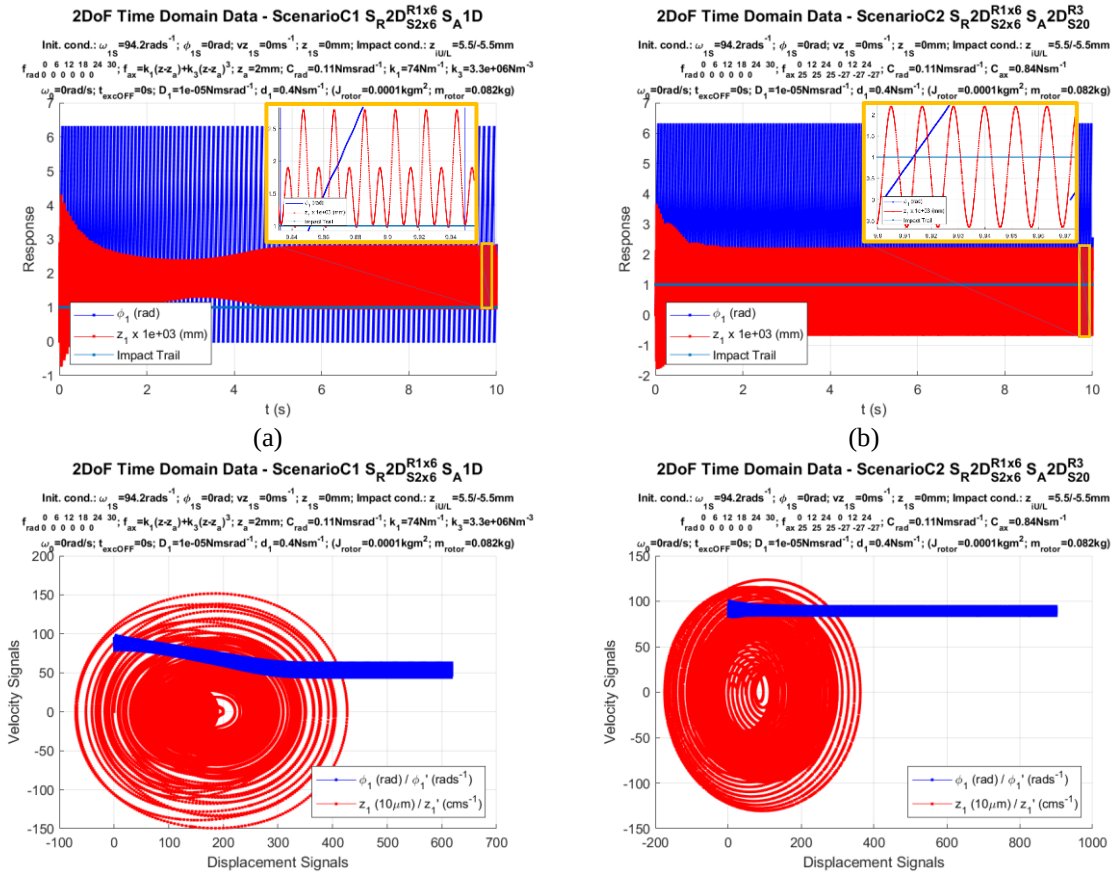

(c) (d)

Fig.17. Same simulation shown as in Fig.16 with same color coding, but rotor displacement $\phi \bmod 2\pi$displayed and z displacement (red) oscillation depicted and dark blue impact trial of axial impact into PM boundaries (here signal kept always =1, no impact occurred and =0, impact in lower or upper boundary present), shown in diagrams (a), (b). For both configuration C1, C2 a resonance relation of $\omega_1 : \omega_2 = 1:1$ seems to be generated. Diagrams (c), (d) show phase space signals.

Let us look at the energies in the system, the kinetic and potential energy as well as the dissipation energy from mechanical friction. The kinetic energy in radial and axial direction is defined as shown in (31) and (32).

$$T_\phi = \frac{1}{2} C_r \phi'^2 \tag{31}$$

$$T_z = \frac{1}{2} m z'^2 \tag{32}$$

The numerically computed potential energy in radial and axial direction for U_ϕ and U_z is shown in (33), (34). Adding up the torque and force signals of all present PM in the according system, here defined as $f_{\Sigma.tr}$, $f_{\Sigma.ta}$ and $f_{\Sigma.Fr}$ adapted from sum signals of equations (23), (24), we can write the potential energies simplified. Note that the axial torque signal is not present in an axial 1D spring system, shown in Fig.12, e.g. $C_a = 0$, but (weakly) present in system of Fig.22.

$$U_\phi = \frac{1}{2} C_r f_{\Sigma.tr}(\phi, z)\phi^2 + \frac{1}{2} C_a f_{\Sigma.Ta}(\phi, z)\phi^2 \tag{33}$$

$$U_z = \frac{1}{2} k_r f_{\Sigma.Fr}(\phi, z) z^2 + \frac{1}{2} k_1 z^2 + \frac{1}{4} k_3 z^4 \tag{34}$$

Also, dissipation due to mechanical friction is given with (35) for torque signal and (36) for the force signal. D_{nl} and d_{nl} are the nonlinear velocity dependent damping functions from used friction model [14] and to obtain the corresponding energy, this signal needs to be multiplied with its corresponding velocity and displacement signal.

$$Q_\phi = D_{nl}(\phi')\phi'\phi \tag{35}$$

$$Q_z = d_{nl}(z')z'z \tag{36}$$

These energy signals are shown in Fig.18 (again for the simulated scenario from Fig.16a). The spring potential from the radial torque signal U_ϕ is growing with time and therefore also the total kinetic and potential energy $T + U$ (Fig.18a). In Fig.18b, the dissipation energies Q_ϕ and Q_z are shown. Only the dissipation of DoF ϕ contributes significantly to the overall system dissipation.

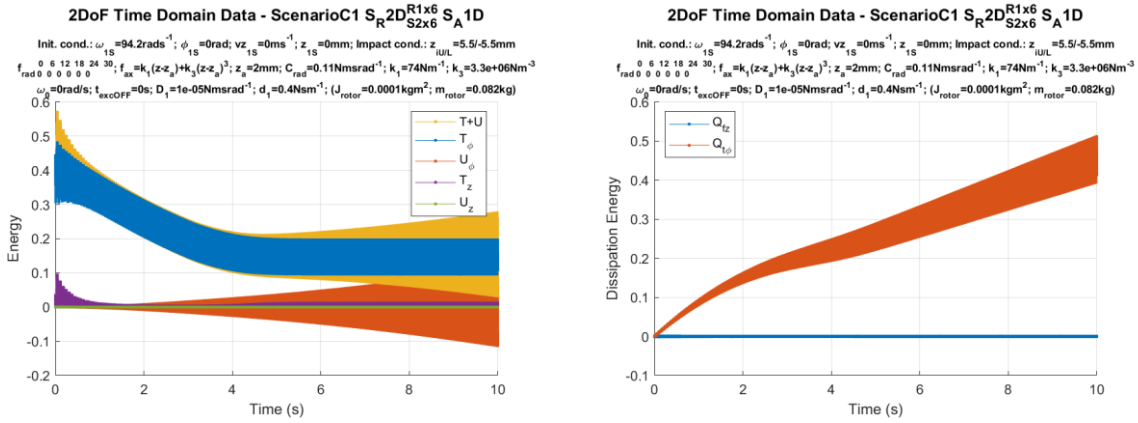

(a) (b)

Fig.18. Kinetic and potential energies (a) and mechanical friction losses (b) in J on simulation shown in Fig.16a.

Shown scenario 3 inFig.19 is the same as Fig.17, but radial and axial damping is set zero. No steady state is reached, as z oscillator starts growing until its amplitude reaches $A = 5.5mm$ where the rotor hits the axially placed stator PM boundary. The impact trial line in diagram (a) drops to zero (impacting occurs) and the KEH system ceases to operate. This behavior is most interesting, as the parametrical excited DoF is expected to grow exponentially. The shown response of DoF z (Fig.19a) shows additionally a superposed beat frequency.

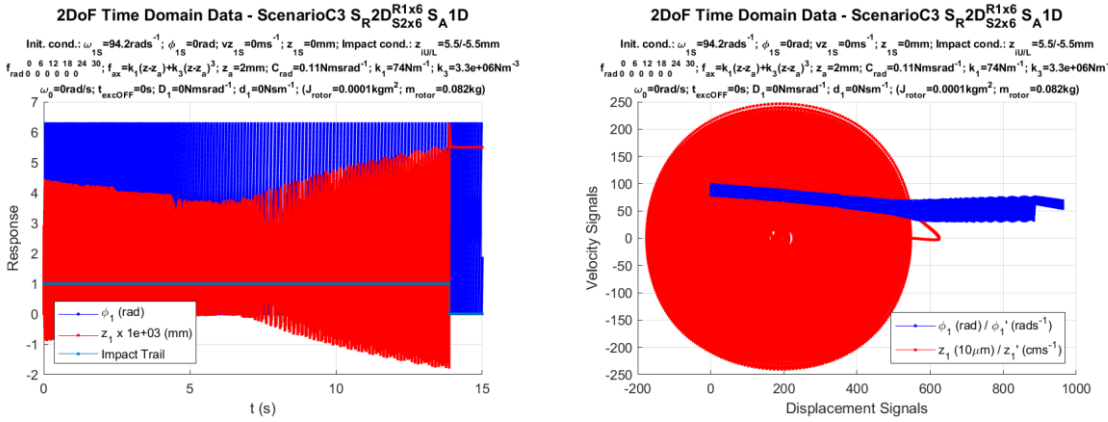

(a) (b)

Fig.19. Same simulation as shown in Fig.17, but radial D_1 and axial friction d_1 set zero. KEH system ceases to operate after z amplitude reaches 5.5mm as it hits axial boundary (a). Diagram (b) shows phase space.

In case of a symmetrically placed axial spring system, simulations show also a steady state oscillation behavior for both axial spring systems (Fig.20a, c). In this case, a resonance at $t \cong 1.47s$ and an amplitude of $A \cong 5.4mm$ is reached before finding at $t > 5s$ a mutually steady state oscillation of ϕ and z.

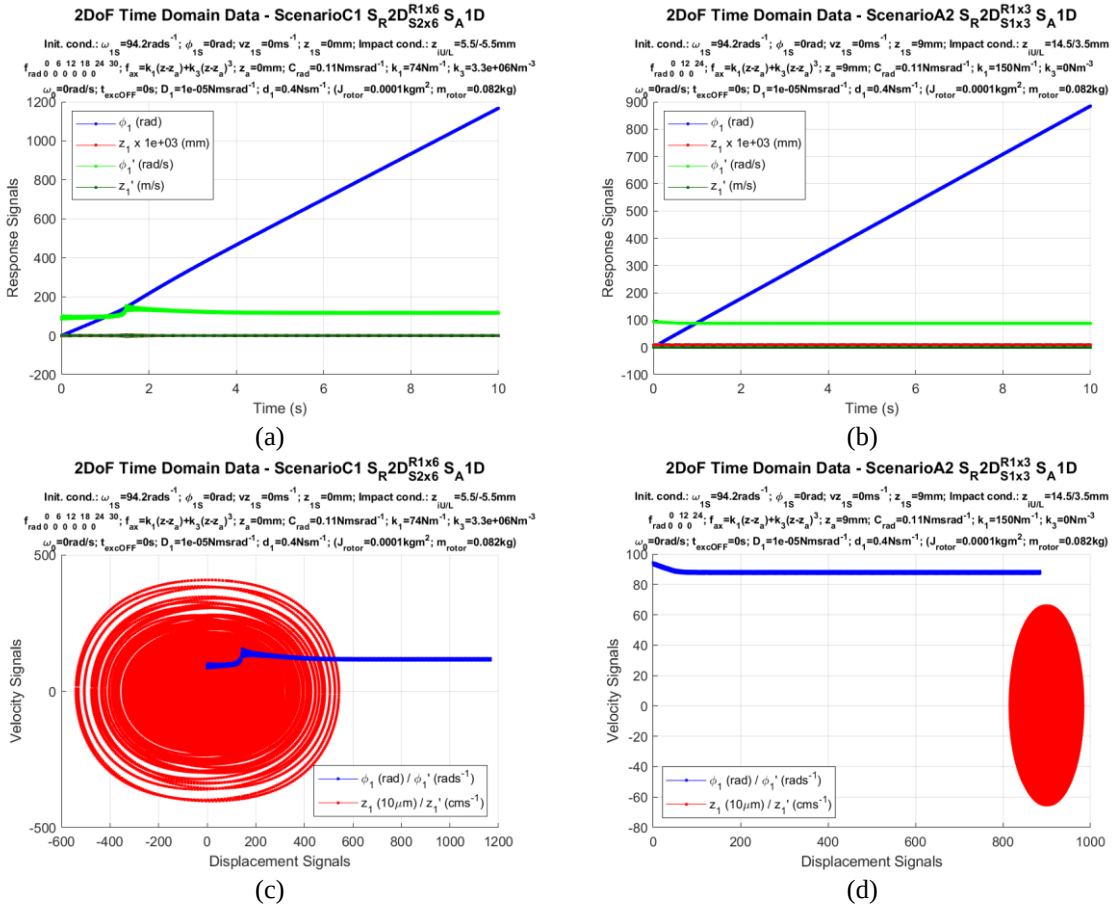

(a) (b) (c) (d)

Fig.20. Situation (a) and (c) show same simulation as shown in Fig.17, but axial spring system placed symmetrical around the origin and situation (b) and (d) showing resulting oscillations with a linear 1D axial spring system.

In case of an asymmetrically placed axial spring system (lumped parameter model situation, Fig.9b), simulations show also a steady state oscillation behavior for both axial spring systems (Fig.20b, d). Interestingly, if only a linear axial spring of $k_1 = 150Nm^{-1}$ is used, the resulting resonance can sustain with only 3 PM stator-rotor pairs radial friction of up $D_1 \cong 30\mu Nmsrad^{-1}$.

4.3 Parameter influence

The following identified realistic parameter set shows the strange phenomenon of reaching a mutually coupled stable resonance. The given comments are for the stator PM distribution shown in Fig.13, and the simulations excerpts shown in Fig.16 – Fig.20.

(1) Axial spring system must not be mandatory placed z axis off-centered. If placed symmetrical, steady state operation canalso be reached (and there are an infinity number of geometrical stator-rotor PM distributions). The original reasoning for a mandatory asymmetry: as larger an asymmetry is made (in a feasible axial z-interval), as more asymmetric torque signal can be generated.
(2) z-interval width: if this interval is set too large, the exponential growing z-amplitude might overcome the axial magnetic force and hard-impact into boundaries is occurring (and cease of operation). For this axial spring system, you have an optimal z-interval width of $11mm$. Interestingly, this asymmetry needs not to be changed when changing revolving direction.
(3) Axial Friction influences the z amplitude and must be carefully chosen and in accordance with the radial and axial stiffness settings. This axial friction parameter d_1 is quite sensitive, for chosen parameter settings (see headings Fig.17).
(4) Changing break torque C_r (and therefore also $k_r = \frac{C_r}{r_0}$), corresponding k_a might be re-set – to keep both oscillators in a common resonance window.
(5) Changing C_r might require changing also the initial ang. velocity condition ω_{1S} to get in a stable operation cycle.
(6) Rotor inertia J influences the drop-rate when starting with a large initial angular velocity condition ω_{1S}. Rotor mass m dictates also amplitude magnitude of z oscillator.
(7) Enlarging radial damping D_1 amplifies DoF z amplitude. Enlarging axial damping d_1 attenuates DoF z amplitude.
(8) Initial conditions of ϕ and z have large influence of resulting beat frequency of z oscillator.

V. Discussion

5.1 Nonresonant mechanical SDoF system

In chapter II we showed that principally an asymmetric (and incommensurable) torque can be generated using disk PMs in nonpolar repulsion techniques. It was verified, that the torque signal of the analytical model and the FE model match well (see also Fig.7). Furthermore, we showed, that such an asymmetric torque signal is described with two parameters, a torque amplitude as well as a positivity. The first parameter is giving the exerted torque over an 2π period and the positivity how large effectively such a torque is used over this period.A given stator-rotor PM distribution with such asymmetric torque signal can be repeatedly applied over the rotor surface and therefore,any present friction can be overcome.

In chapter III it follows, that applying this 2π periodic torque signal in a most simple radial mechanical SDoF system using a cam in axial direction on a rotating shaft, an apparent perpetual shaft motion is generated. Creating an harmonic cam with the given parameters is challenging to build.

5.2Resonant mechanical 2DoF system

A mechanical 2DoF system with an attached electrical transducer has been modeled in chapter 4. Here we went a different way and placed again a geometrical disk PM configuration on the stator-rotor system with its radial DoF ϕ. In addition, instead of using a cam function as done in chapter 3, we let this 2nd DoF oscillate freely in axial direction z; to do so, an additional axial spring system needs to be present. Two lumped parameter models with such axial spring systems have been modeled (Fig.13 and Fig.23) and simulated (Fig.16 –Fig.20). It could be shown, that both systems, using the same symmetrical rotor PM distribution (all magnets in the same plane) and similar but not the same axial PM distributions might find coupled interlocked resonances to create also an apparent perpetual shaft motion.

In this system we deal with two displacement-coupled DEs that form for the radial DoF a torque Hill DE(28)as well as for the axial DoF a force Hill DE (29). This model stems from the FE simulated torque and force signal and their Fourier series approximations creating a radial 2D PM spring function.

These simulations have been partially validated in other projects, namely the torque signal of a nonpolar magnetic repulsion system (compare also Fig.1a).

The simulated systems distinguish themselves with remarkable realistic parameter settings and – as in many of already such lumped modeled parameter systems – all those parameters can be changed in a rather large and realistic interval. The key parameters of such systems are the stiffness- and damping-terms, which define the coupled oscillation behavior. The exact parameter setting for achieving best coupled ϕ and z resonances could not be identified, however, we listed in tedious system simulations for the time being in chapter 4.3 all parameters and their influences on the overall system behavior.

VI. Conclusions

In this work we laid out a most simple macroscopic model for two displacement coupled parametric oscillators by means of nonpolar magnetic repulsion systems. It could be shown, that the two such coupled

oscillators with a most basic mechanical setup form for both mechanical degrees of freedom Mathieu (Hill) equations. Those Mathieu equations are formed using Fourier series approximation of torque and force signals, generated by a set of a geometrical distributed stator-rotor PMs. There are infinity sets of PM distributions, one that works exceptionally well to demonstrate the apparent perpetual motion effect is the radial PM distribution of Fig.13. Even though the system is most simple – just a rotating and axially sliding rotor – the resulting stiffness term is complex and necessary to generate an asymmetric torque signal. The simulation was performed with numerical tools and verified with many numerical solvers, simulation times of up to $500s$to show stable steady state oscillations and step sizes down to 10^{-12}s that the integrators work as specified. The lumped parameter model has six main system parameters:J, m, D, d, C and k plus a carefully developed distribution of PM lineup on the stator and rotor surface. Also, important for an apparent stable perpetual oscillation, is the asymmetric axial spring distribution, which seems to increase an asymmetric torque generation on the rotor shaft. Moreover, most realistic parameter characteristics have been chosen in the model and those system values can be also modified in a rather large interval which makes this system intriguingly interesting.

However, as we simulate this system with (nonlinear) mechanical damping for both degrees of freedom, we run straight into the problem of the energy source. We are currently investigating several tracks for explaining this artefact. A most promising theory of classical quantum mechanics is given in [16], in which also the ionization energies for the first 20 atoms of the periodic system have been validated. Applying carefully the shown equations for complex NdFeB PMs, it might be possible to explain this simulation artefact. This manuscript must be regarded currently as a modeling artefact and intends to reach out to research groups to investigate together phenomena of this kind.

VII. Appendix A – Creation Of A Spring Potential

In this appendix, the spring potential for a 2D radial PM spring from chapter II is presented. The spring energy of a linear or nonlinear spring might be calculated using (37). Inserting for instance a linear spring function with displacement x and stiffness k(38), its potential becomes(39).

$$U_S = \int F_S(x)dx \tag{37}$$

$$F_S(x) = k\,x \tag{38}$$

$$U_S = \int F_S(x)dx = \int k\,x\,dx = \frac{1}{2}k\,x^2 \tag{39}$$

Using the same formalism for the obtained 2D radial PM spring and approximating it with a first order harmonic approximation for its radial $\tau_\phi(\phi)$(40) and axial $\tau_z(z)$(41) torque, given the according interval of approximation for the corresponding direction α (°) and z (mm), see also Fig.21a, we might write the potential as shown in (43).

$$\tau_\phi(\phi) = \sin\left(\frac{\pi}{\alpha}\phi\right) \tag{40}$$

$$\tau_z(z) = \frac{1}{2}\left(1 + \cos\left(\frac{\pi}{\beta}z\right)\right) \tag{41}$$

$$\tau_{\phi z}(\phi, z) = \sin\left(\frac{\pi}{\alpha}\phi\right)\frac{1}{2}\left(1 + \cos\left(\frac{\pi}{\beta}z\right)\right) \tag{42}$$

$$U_S \overset{?}{=} \int \tau_\phi(\phi)d\phi \int \tau_z(z)dz = -\frac{\alpha}{2\pi^2}\cos\left(\frac{\pi}{\alpha}\phi\right)\left(\pi z + \beta\sin\left(\frac{\pi}{\beta}z\right)\right) \tag{43}$$

The obtained 3D plot for such a potential (43) is given in Fig.21b. Back calculating the potential from (13) (second term) for the according DoF will not result in the original function given in (42).

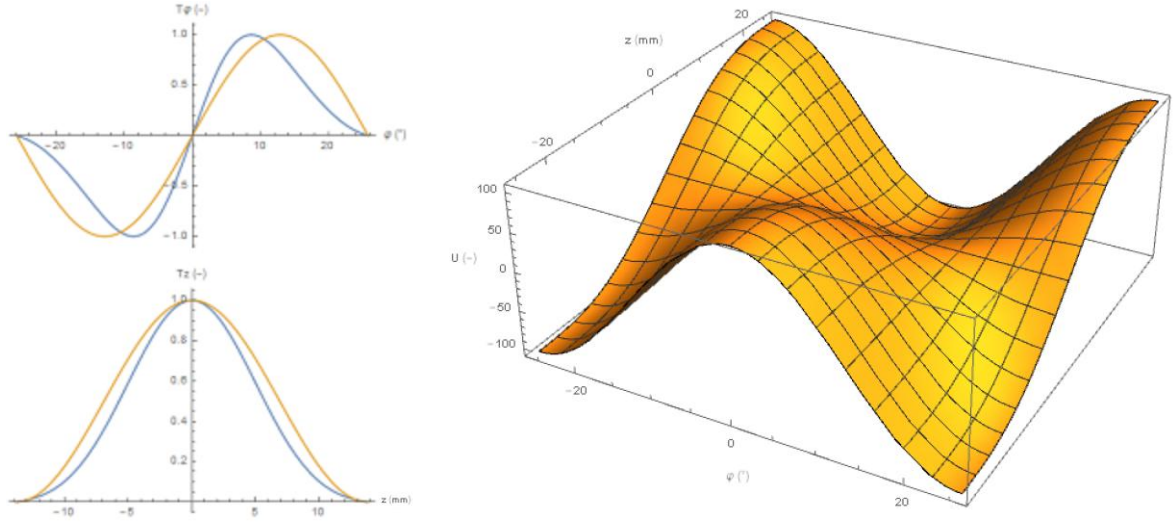

(a) (b)

Fig.21. 1st order harmonic approximations (orange) of normalized 4th order Fourier torque radial τ_ϕ and axial τ_z signals (blue) in (a), data used from Fig.3 and its attempted potential function in a 3D plot with its independent parameters ϕ and z in (b).

VIII. Appendix C – Alternative Model Of Axial Spring Implementation

The torque and force signal for axially placed PM batteries with diameter 6mm and length 6mm is displayed in Fig.22 – like the Fig.13 (where a radial PM battery is shown).

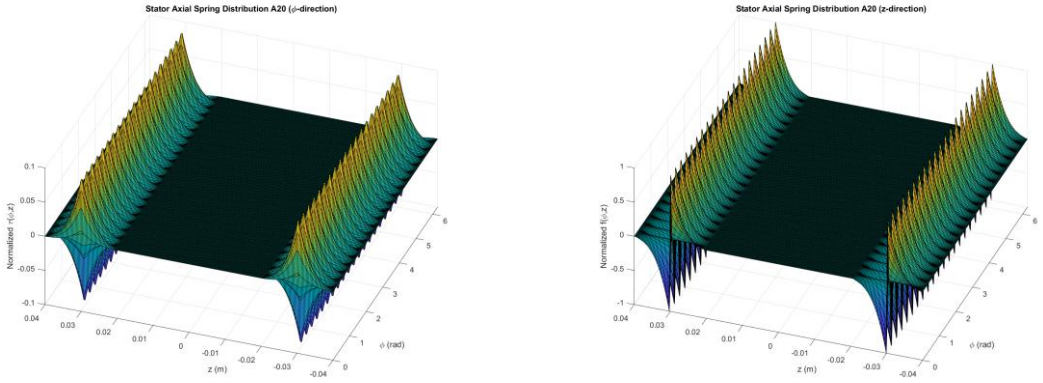

(a) (b)

Fig.22. Diagram (a) shows axial-torque and (b) -force signal of stator PM batteries with 20 PMs on each side. Note that in (a) the created normalized torque is weak and only ca. 10% of its force signal counterpart. The much smaller torque signal is the result of the chosen geometrical distribution of the 20 PM magnets. They are aligned axially on a radius on the stator sidewalls and are so close together, that a rotor PM flyby will exert only little torque signal.

Such axial PM batteries (here are 40 PMs on the stator) can also be used as an axial spring system. Fig.23shows lumped parameter model of a KEH, using a more complex axial spring system. On the rotor, there might be only a few PMs present.

Such axial PM batteries (here are 40 PMs on the stator) can also be used as an axial spring system. Fig.23shows lumped parameter model of a KEH, using a more complex axial spring system. On the rotor, there might be only a few PMs present.

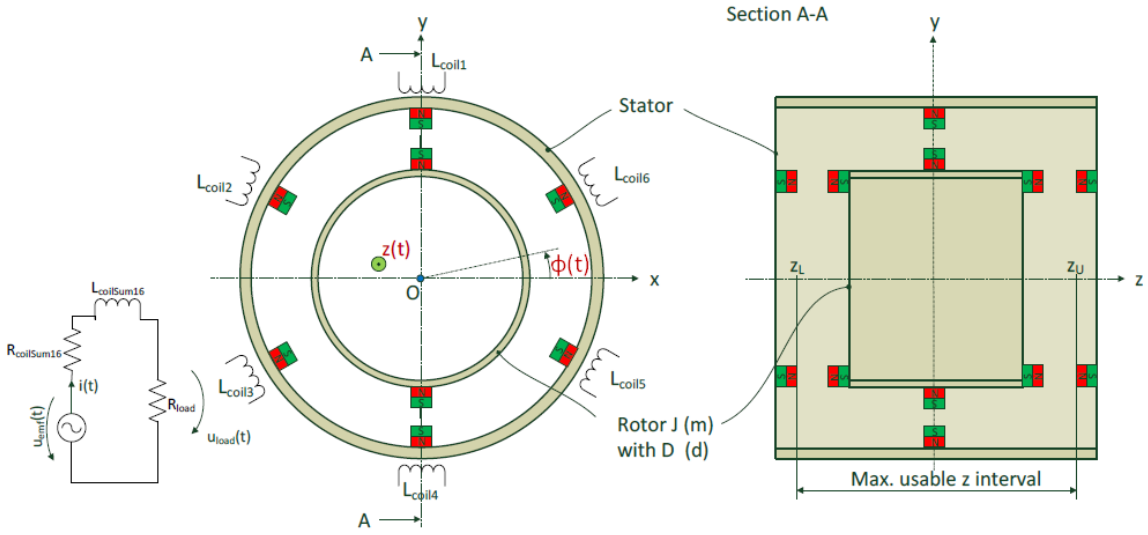

Fig.23. Lumped parameter model of 2DoF KEH system with a rotating $\phi(t)$ axially $z(t)$ moving rotor on a hollow shaft without bearings and a more elaborate axial PM distribution (compare this model to Fig.12).

The corresponding DE system from chapter 0, equation (23)-(25) needs be adapted accordingly, represented in the following set:

$$J\phi'' + D\,(\phi' - \omega_0) + C_r \sum_{n=1}^{n_{PMr}} f_{\tau rad}\,(\phi - \phi_n, z - z_n) + C_a \sum_{n=1}^{n_{PMa}} f_{\tau ax}\,(\phi - \phi_n, z - z_n) + \varepsilon_\phi\, i = 0 \qquad (44)$$

$$m\,z'' + d\,z' + k_r \sum_{n=1}^{n_{PMr}} f_{Frad}\,(\phi - \phi_n, z - z_n) + k_a \sum_{n=1}^{n_{PMa}} f_{Fax}\,(\phi - \phi_n, z - z_n) + \varepsilon_z\, i = 0 \qquad (45)$$

$$L_{coilSum\ 16}\, i' + (R_{coilSum\ 16} + R_{load})\, i = \varepsilon_\phi\, \phi + \varepsilon_z\, z \qquad (46)$$

In (44), the last sum term with amplification radial stiffness factor C_a is inserted, as placed axial PM sets exert also a torque signal and in (45) the nonlinear stiffness term is replaced by the corresponding axial sum force function with amplification axial stiffness factor k_a. Unchanged equation (46) just given for the completeness of the DE set. Note that the axial PM battery set needs also to be placed off-centered (with same distance as z_{asym} to create similar oscillation characteristics as with model shown in lumped parameter model of Fig.12).

IX. Appendix D – Implementation Of Impacting (For Resonant KEH Type)

Nonlinear system deal often also with impacting and there are several models for impacting, see for example [17], [9]. Even though for continuous steady state operations impacting in axial boundaries never occur in the resonant KEH system, it is useful to have such an impact model in place, to investigate the limitations of a system. In early models, we used even impacting to investigate steady state operations. Such continuous steady state operations might be simulated successfully, but whether such system can be built successfully is unlikely, as on hard or also soft-impacting, much energy is dissipated. Equation (47) shows the probably most simple and very successful parameter model for a hard or soft impact. In this shown example, we deal with a mass m that is only accelerated by the gravitational field g and impacts on $y = 0$. The impact characteristic is modeled with a (translational) damping d and stiffness k parameter.

$$-mg = \begin{cases} my'' + dy' + ky, & y < 0 \\ my'', & y \geq 0 \end{cases} \qquad (47)$$

This implementation is most efficiently done in MATLAB Simulink using a switch, as shown in Fig.24.

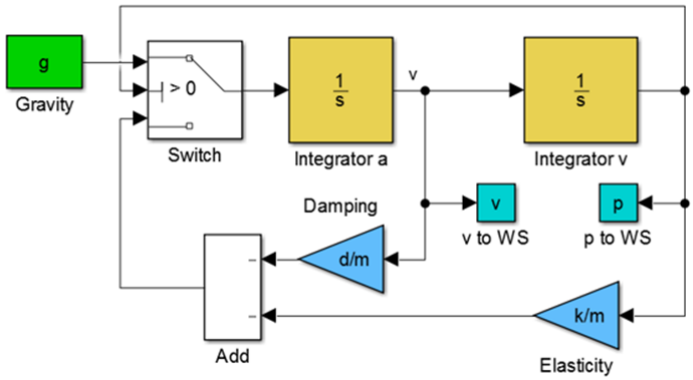

Fig.24.Simple and most robust MATLAB Simulink impact model

X. Appendix E – Tu Eindhoven Yildiz Motor Measurements

The load curve of the Yildiz motor is depicted in Fig.25a. It starts at 2485rpm (no-load) and drops quite linearly (considering the precision of the measurement instrument) to 2100rpm (45W load).

A linearly extrapolated load curve of the results of Fig.25a is given in Fig.25b. A theoretical maximum power could be delivered by this measured prototype of around 300W, see also [12] for additional details.

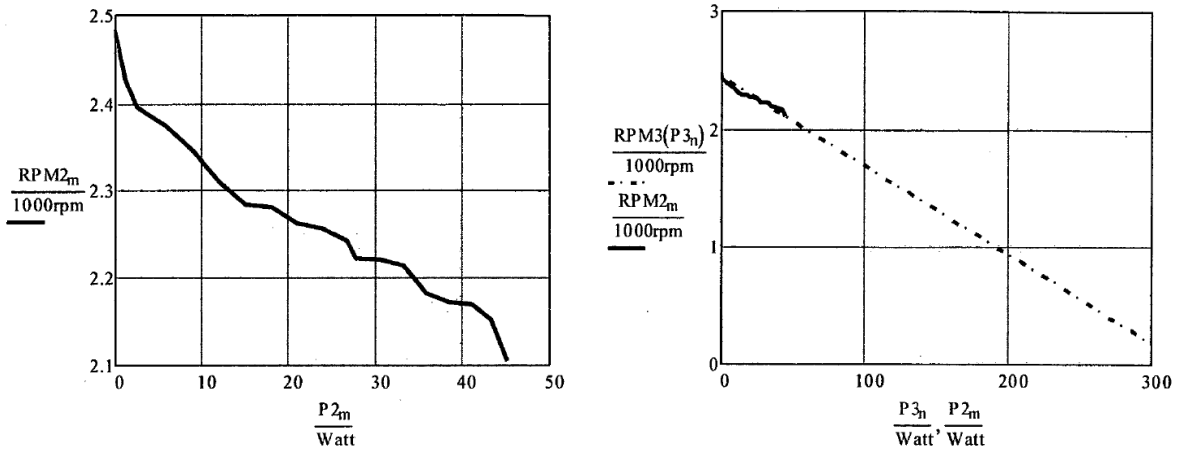

(a) (b)

Fig.25. Rotor speed (rpm) as a function of the delivered power (W) in (a) and the linear extrapolated motor characteristics (b) – excerpt of [12].

References

[1]. M. Yildiz, "Device having an arrangement of magnets", WO 2009/019001 A3 2009/019001 A3.

[2]. A. D. T. Elliott, L. M. Miller, E. Halvorsen, P. K. Wright, and P. D. Mitcheson, "Which is better, electrostatic or piezoelectric energy harvesting systems?," *J. Phys.: Conf. Ser.*, vol. 660, p. 12128, 2015.

[3]. P. D. Mitcheson, E. M. Yeatman, G. K. Rao, A. S. Holmes, and T. C. Green, "Energy Harvesting From Human and Machine Motion for Wireless Electronic Devices," *Proc. IEEE*, vol. 96, no. 9, pp. 1457–1486, 2008.

[4]. F. U. Khan, "Review of non-resonant vibration based energy harvesters for wireless sensor nodes," *Journal of Renewable and Sustainable Energy*, vol. 8, no. 4, p. 44702, 2016.

[5]. D. P. Arnold, "Review of Microscale Magnetic Power Generation," *IEEE Trans. Magn.*, vol. 43, no. 11, pp. 3940–3951, 2007.

[6]. S. P. Beeby *et al.*, "A micro electromagnetic generator for vibration energy harvesting," *J. Micromech. Microeng.*, vol. 17, no. 7, pp. 1257–1265, 2007.

[7]. E. Arroyo and A. Badel, "Electromagnetic vibration energy harvesting device optimization by synchronous energy extraction," *Sensors and Actuators A: Physical*, vol. 171, no. 2, pp. 266–273, 2011.

[8]. B. P. Mann and N. D. Sims, "Energy harvesting from the nonlinear oscillations of magnetic levitation," *Journal of Sound and Vibration*, vol. 319, no. 1-2, pp. 515–530, 2009.

[9]. Y. Jia, "The Convergence of Parametric Resonance and Vibration Energy Harvesting,"

[10]. L. Kurmann *et al.*, "Autoparametric Resonance Systems for Vibration-Based Energy Harvesters," *J. Phys.: Conf. Ser.*, vol. 660, p. 12070, 2015.

[11]. L. Kurmann, Y. Jia, Y. Manoli, and P. Woias, "Magnetically levitated autoparametric broadband vibration energy harvesting," *J. Phys.: Conf. Ser.*, vol. 773, p. 12006, 2016.

[12]. J.L. Duarte, "Introducing the Yildiz Motor & Modeling the Yildiz Motor," in *Non-patent literature (EZ81K3II8231020) cited during the examination procedure of Application no 08801521 with reference to "EP2153515 Device Having an Arrangement of Magnets" by M. Yildiz, WIPO Patent Collections*, 2017.

[13]. D. J. Griffiths, *Introduction to electrodynamics,* 3rd ed. Upper Saddler River, N.J.: Prentice Hall; London : Prentice-Hall International, 1999.

[14]. M. Charu, D. Warren, S. Wallace, and H. Guoqiang, *A New Continuously Differentiable Friction Model for Control Systems Design*. Piscataway N.J.: IEEE, 2005.

[15]. D. Spreemann and Y. Manoli, *Electromagnetic Vibration Energy Harvesting Devices: Architectures, Design, Modeling and Optimization*. Dordrecht: Springer Netherlands, 2012.

[16]. R. L. Mills, "Exact Classical Quantum-Mechanical Solutions for One- through Twenty-Electron Atoms," *Physics Essays*, vol. 18, no. 3, pp. 321–361, 2005.

[17]. R. I. Leine, D. H. van Campen, and C. H. Glocker, "Nonlinear Dynamics and Modeling of Various Wooden Toys with Impact and Friction," *Journal of Vibration and Control*, vol. 9, no. 1-2, pp. 25–78, 2003.

Lukas Kurmann. "Oscillators with Nonpolar Magnetic Repulsion System and its Use in Rotary Nonresonant and Resonant Kinetic Energy Harvesters." IOSR Journal of Applied Physics (IOSR-JAP) , vol. 10, no. 4, 2018, pp. 57-76.